Study of surface roughness on flow past a wind turbine tower section

Vimalkumar, Shyam; De Tavernier, Delphine; Von Terzi, Dominic; Belloli, Marco; Viré, Axelle

DOI
10.1088/1742-6596/2767/2/022063

Publication date
2024

Document Version
Final published version

Published in
Journal of Physics: Conference Series

Study of surface roughness on flow past a wind turbine tower section

Journal of Physics: Conference Series **2767** (2024) 022063 doi:10.1088/1742-6596/2767/2/022063

Study of surface roughness on flow past a wind turbine tower section

Shyam VimalKumar[1], Delphine De Tavernier[1], Dominic von Terzi[1], Marco Belloli[2], Axelle Viré[1]

1 Faculty of Aerospace Engineering, Delft University of Technology, The Netherlands
2 Department of Mechanical Engineering, Politecnico di Milano, Italy

E-mail: s.vimalkumar@tudelft.nl

Abstract. The flow around wind turbine towers usually reaches very high Reynolds numbers greater than a million. Understanding the flow around the towers under these conditions is crucial, as it may lead to vibrations due to the vortices formed. Investigating aerodynamic characteristics at such high Reynolds numbers, both numerically and experimentally, is challenging. The current study validates such an experimental study, where a rough surface is employed to increase the effective Reynolds numbers and accelerate the laminar-turbulent transition in the boundary layer. Unsteady Reynolds-Averaged Navier-Stokes (RANS) simulations are carried out using OpenFOAM for a Reynolds number range of $1.36{\cdot}10^5$ to $6.8{\cdot}10^5$. The constant (a_1) used to calculate the eddy viscosity is varied to simulate the flow separation during adverse pressure gradients. A force partitioning method is implemented in OpenFOAM and various force contributions are analysed for this Reynolds number range. It is seen that the RANS simulations overpredict the aerodynamic characteristics and the extent of flow separation unless the value of a_1 is varied as a function of the Reynolds number. Furthermore, it is observed that the only force contributor is the vorticity-induced force, as the simulations are performed for a fixed cylinder.

1. Introduction

In recent times, the size of wind turbines has increased to reduce the cost of energy per wind turbine. Even though there is a greater advantage in efficient energy production, additional care must be taken during the installation of the turbines. Larger wind turbines lead to taller wind turbine towers. These are prone to aerodynamic instabilities when they stand upright without the rotor-nacelle assembly, especially when standing upright at the quay-side, during transportation on a vessel, or while on the foundation during installation. Vortex-induced vibrations (VIV) are one such phenomenon that potentially leads to structural fatigue of the tower.

As the turbine towers are large structures, the Reynolds number reaches trans-critical regimes ($Re > 3.5 \cdot 10^6$) at usual wind speeds. In this condition, the flow transitions from laminar to turbulent already in the boundary layer before separation, as studied by Roshko [1]. Previous studies also show that vortex shedding reappears in the trans-critical flow regime as seen in the sub-critical Reynolds numbers ranges [2]. However, investigating the aerodynamic characteristics at such high Reynolds number flows is often challenging due to the difficulty in setting up numerical simulations or experiments and resource availability. Nevertheless, it is observed in

other studies that surface roughness can be used to accelerate the laminar-turbulent transition in the boundary layer [3; 4] and, hence, may be used to mimick high Reynolds number phenomena at a considerably lower Reynolds number. As observed in the detailed study of van Hinsberg [5], the 'drag crisis' is seen at a lower Reynolds number for the rough cylinder. Furthermore, the minimum drag coefficient after the critical flow state is higher for rough cylinders than that observed for smooth circular cylinders, which is similar to the findings from Belloli et al. [2].

In addition to experimental studies, several numerical investigations on flow over rough cylinders were carried out. Most of the previous works concentrated on Reynolds-Averaged Navier-Stokes (RANS) simulations for subcritical Reynolds numbers [6; 7]. Fuzaro Rafael et al. [8] proposed mathematical models to accurately predict the laminar-turbulent transition, which is challenging, especially at high adverse pressure gradients (APG) as seen for flows over cylinders or thick airfoils. Gutierrez et al. [9] conducted an extensive study on predicting flow separation over thick airfoils with leading-edge roughness. As can be seen in the study, a correction in the calculation of eddy viscosity μ_t is employed as often turbulent shear stresses are overpredicted near the airfoil. Mendez at al. [10] performed similar studies to analyse flow over airfoils with leading-edge roughness using various roughness models like the Hellsten and Laine model [11], and the model by Knopp et al. [12]. These models are well-suited for predicting airfoil aerodynamic characteristics with a distributed rough surface over the airfoil.

A recent study on VIV of a smooth wind turbine tower section at a trans-critical Reynolds number shows a continuous exchange of energy from fluid to structure and vice-versa near the natural frequency [13]. Menon et al. [14] demonstrate how the force partitioning method can offer a more detailed understanding of the forces acting on the structure under various flow conditions. This is particularly valuable because the structure's shape significantly influences the forces acting upon it and can help design effective mitigation techniques against VIV.

Introducing surface roughness to the structure may lead to different force implications within the Reynolds number regime. Hence, the current study focuses on predicting the force coefficients and flow separation over rough tower sections using the above-mentioned correction methods. A first-hand analysis of the forces acting on the cylinder section will then be analysed further using the force-partitioning method for Reynolds number ranging from $1.35 \cdot 10^5$ to $7 \cdot 10^5$.

2. Methodology

2.1. Numerical Methods

The numerical simulations are carried out for a two-dimensional cylinder section in the open-source software OpenFOAM-v2012 [15]. As the flow field is in the turbulent regime, the unsteady Reynolds-averaged Navier–Stokes (URANS) equations are solved using the two equation turbulence model $k-\omega$ SST [16]. Turbulent kinetic energy, k, and specific dissipation rate, ω, can be modified to get higher skin friction and simulate the roughness effect. In the SST model, the turbulent shear stress in the boundary layer is limited to avoid over-estimation of shear stress from Boussinesq eddy-viscosity models. Such a limiter to eddy viscosity is added to the SST model using the equation:

$$\mu_t = \frac{a_1 \rho k}{\max(a_1 \omega; |\Omega| F_2)}, \tag{1}$$

where $a_1 = 0.31$, $|\Omega|$ is the magnitude of strain rate tensor and F_2 is a blending function in the turbulence model as shown below:

$$F_2 = \tanh\left(\left(\max\left(\frac{2\sqrt{k}}{\beta^* \omega y}, \frac{500\nu}{y^2 \omega}\right)^2\right)\right), \tag{2}$$

where $\beta^* = 0.09$ and y is the first cell height. For the implementation of the Wilcox boundary condition to simulate flow over rough surface, the specific dissipation rate, ω, is modified as:

$$\omega = \frac{u_\tau^2}{\nu} S_R. \tag{3}$$

The non-dimensional term S_R is defined as:

$$S_R = \begin{cases} (50/h_s^+)^2 & \text{for } h_s^+ < 25 \\ (100/h_s^+) & \text{for } h_s^+ > 25 \end{cases} \tag{4}$$

The normalised roughness height h_s^+ is defined as $h_s^+ = h_s u_\tau / \nu$, where u_τ is the friction velocity and h_s is the equivalent roughness height. From the works of Hellsten and Laine, a correction term F_3 is activated in the SST model, which modifies Equation (1) [11]. The term F_2 is then multiplied by F_3, which is defined as:

$$F_3 = 1 - \tanh\left(\left(\frac{150\nu}{\omega y^2}\right)^4\right). \tag{5}$$

The Wilcox boundary condition and the Hellsten's correction are then implemented in OpenFOAM and employed to accurately simulate the flow over a rough cylinder.

2.2. Modification of a_1

As per the Johnson-King model, the ratio of turbulent shear stress τ and the turbulent kinetic energy is defined as a constant called a_1 [17]. On the other hand, in two-equation models, the shear stress is calculated as $\tau = \mu_t \Omega$. As explained in the work of Menter [18], in APG flows, this equation leads to an overprediction of τ as the production is significantly larger than the dissipation. Hence, Equation (1) guarantees that the equation used for the regions with APG is $\mu_t = a_1 \rho k / |\Omega| F_2$, whereas in the rest of the boundary layer, the equation $\mu_t = \rho k / \omega$ is employed.

A similar corrective method is used in Matyushenko et al. [19] and Gutierrez et al. [9], where a lower value of a_1 helps to capture the flow separation on a thick airfoil more accurately. By lowering the value of a_1, the turbulent viscosity is reduced and, consequently, the turbulent friction near the wall. Flow separation is promoted in such a case and potentially leads to higher drag.

2.3. Force-partitioning method

The method of force-partitioning is based on the work of Quartappelle and Napolitano [20], which was further extended by Zhang et al. [21] and Menon and Mittal [14]. In this method, the Navier-Stokes momentum equation is projected on the gradient of a harmonic function $\phi^{(i)}$. The partitioned forces are obtained upon integration over the fluid domain V_f. The partitioned forces contain contributions from added mass (F_K), vorticity (F_ω), viscosity (F_σ), potential flow (F_ϕ) and the forces due to flow and vortices at the outer boundary of the domain (F_Σ). The resulting force acting on the body can then be written as:

$$\begin{aligned} F_B =& F_K + F_\omega + F_\sigma + F_\phi + F_\epsilon \\ F_B =& \underbrace{-\rho \int_B \vec{n} \cdot \frac{d\vec{U_B}}{dt} \phi^{(i)} dS - \rho \int_B \frac{1}{2} U_B^2 \vec{n} \cdot \nabla \phi^{(i)} dS}_{\text{kinematic force}} \end{aligned}$$

$$+\underbrace{\rho\int_{V_f}\nabla\cdot(\vec{\omega}\times\vec{u})\phi^{(i)}dV+\rho\int_{V_f}\nabla^2\left(\frac{1}{2}u_\nu^2+\vec{u_\phi}\cdot\vec{u_\nu}\right)\phi^{(i)}dV}_{\text{vortex-induced force}}$$
$$+\underbrace{\mu\int_B(\vec{\omega}\times\vec{n})\cdot\vec{\nabla}(\phi-\hat{e}_i)dS}_{\text{viscous force}}+\underbrace{\rho\int_{V_f}\nabla^2\left(\frac{1}{2}u_\phi^2\right)\phi^{(i)}dV}_{\text{potential flow force}}$$
$$-\underbrace{\rho\int_\Sigma\frac{d\vec{U}}{dt}\cdot\vec{n}\phi^{(i)}dS+\mu\int_\Sigma(\vec{\omega}\times\vec{n})\cdot\nabla\phi^{(i)}dS}_{\text{force due to flow and vortices at outer boundary}}, \tag{6}$$

where B represents the surface of the body and Σ represents the outer boundary of the domain. The velocity of the body at every point is represented as U_B. The velocity components u_ϕ and u_ν are the curl-free and divergence-free components of velocity as shown in Equation (7) [22]:

$$\vec{u}=\vec{u_\phi}+\vec{u_\nu}=\nabla\Phi+\nabla\times\vec{A}, \tag{7}$$

where Φ and $\vec{A}$ are scalar and vector potentials, respectively.

The partitioned forces are implemented in OpenFOAM, where *pimpleFoam* is modified to calculate the harmonic function for each time step. The force coefficients are then calculated as a *functionObject*, which can be later accessed for post-processing [23].

2.4. Simulation setup

The schematic representation of the system used in the simulations and the mesh are shown in Figure 1. In the current study, flow over a fixed rough cylinder is carried out. In order to verify the numerical model employed, the results from the experiment performed by Belloli et al. [2] is compared to the numerical simulation results.

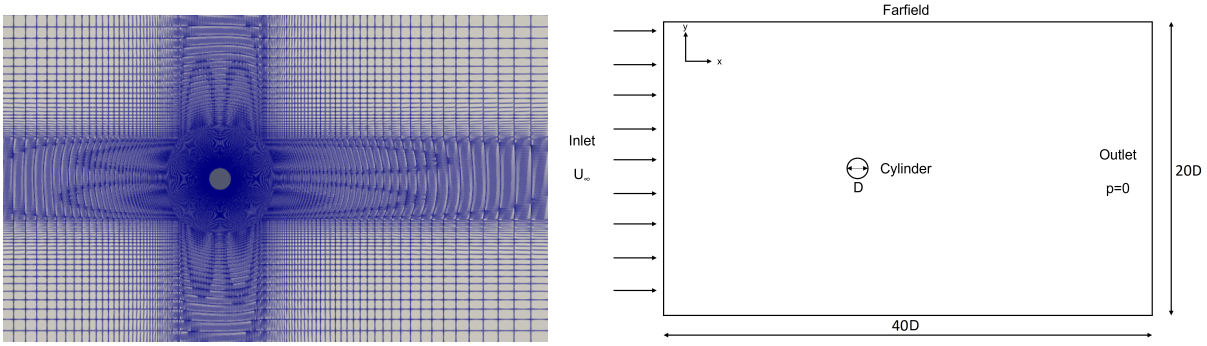

Figure 1: Schematic representation of the computational domain: Cartesian mesh (left), domain characteristics (right).

The structured grid for the computational domain is generated using *blockMesh* module in OpenFOAM. The first cell height of the mesh, y_{wall}, is $8\cdot10^{-5}$ m, satisfying the near-wall dimensionless distance, y^+, to be less than 1. A mesh independence study is carried out to finalise the mesh size, and the total number of elements of the mesh is $3.01\cdot10^5$. The time step size was varied to keep the Courant-Friedrichs-Lewy (CFL) number equal to 2. The parameters used in the simulation is shown in Table 1.

As OpenFOAM is designed for three-dimensional space, the mesh is three-dimensional in nature, extending to a thickness of one cell in the z-direction, as outlined in Table 1. The initial

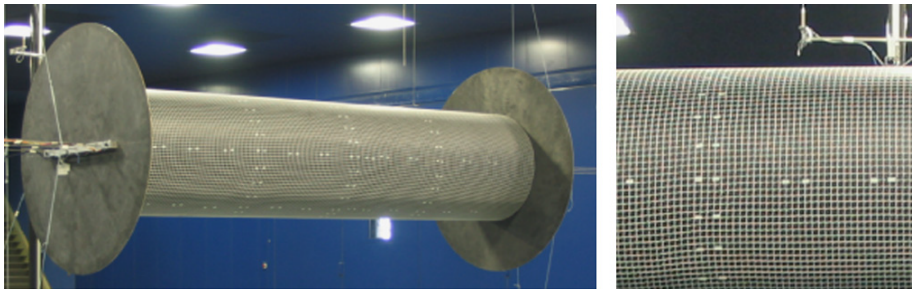

Figure 2: Experimental setup of the rough cylinder. Image taken from Belloli et al. [2].

Variables	Parameters
Diameter, D [m]	0.72
Height, z [m]	1
Roughness ratio, k_s/D	0.002
Turbulence intensity, TI	0.02
Reduced velocity, U_{red}	2.02 - 10.25
Reynolds number, Re	$1.36 \cdot 10^5$ - $6.86 \cdot 10^5$

Table 1: Parameters used for the simulations of the rough cylinder.

values for the turbulence parameters, turbulent kinetic energy k and turbulent dissipation rate ω are calculated using the Equation (8), where μ_t/μ is taken as 10.

$$\begin{aligned} k &= \frac{3}{2}(TI \cdot U_\infty)^2, \\ \omega &= \frac{\rho k}{\mu}\left(\frac{\mu_t}{\mu}\right)^{-1} \end{aligned} \tag{8}$$

These parameters at the cylinder boundary are taken as $k = 10^{-10} m^2/s^2$ and ω is calculated as

$$\omega = \frac{6\mu}{\beta_1 y_{wall}^2}, \tag{9}$$

where $\beta_1 = 0.075$ [18]. During the experiment conducted by Belloli et al. [2], the surface roughness was increased by adding a nylon net to the smooth cylinder which created a roughness ratio of 0.2%, as is shown in Figure 2. Therefore, a uniform roughness distribution is assumed for the numerical simulation with the above mentioned roughness ratio.

3. Results

In the section, the numerical simulations are validated against the steady results from the experimental study conducted by Belloli et al. [2]. The numerical parameters chosen for the study are mentioned in Table 1. The turbulence model is chosen to be $k-\omega$ SST, as this model is understood to be one of the best-performing numerical models to simulate flows with adverse pressure gradients [16].

3.1. Initial results with $k-\omega$ SST

The initial studies are carried out using the $k-\omega$ SST model with a rough-wall-function for ω to simulate the surface roughness Figure 3 compares force coefficients obtained from simulations using $k-\omega$ SST without the Wilcox boundary condition. The drag coefficients obtained from

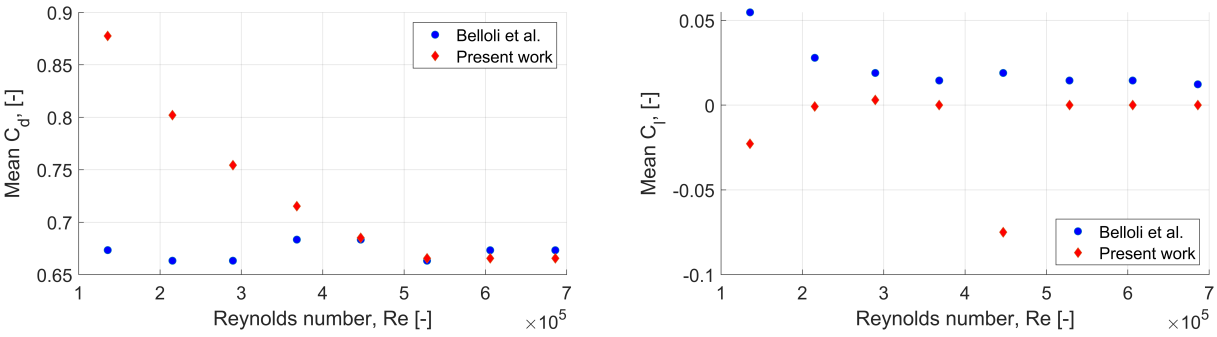

Figure 3: Variation of mean drag coefficient and mean lift coefficient for a fixed cylinder at different Reynolds numbers without using the Wilcox Boundary condition, compared against experimental results from [2].

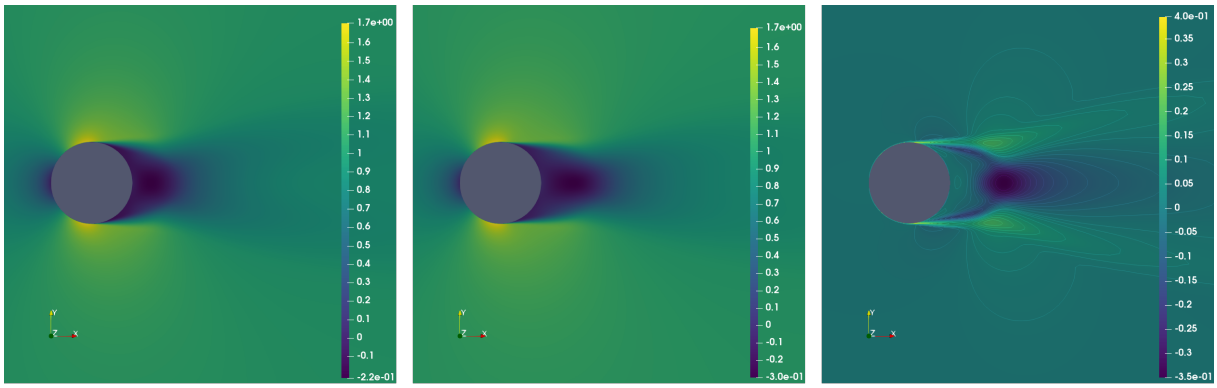

Figure 4: Normalised streamwise-velocity component on the rough cylinder: (a) $Re = 1.36 \cdot 10^5$, (b) $Re = 6.86 \cdot 10^5$, and (c) the difference in normalised streamwise-velocity component between both Reynolds numbers.

the experiment are pressure drag as friction drag is observed to be negligible at these Reynolds number ranges [4]. It can be clearly seen that the turbulence model overpredicts the drag coefficient for Reynolds numbers less than $\approx 4 \cdot 10^5$. The maximum error estimated in predicting the mean drag coefficient is around 30%. Even though the drag coefficients are predicted accurately for flows at higher Reynolds numbers, a significant difference in the recirculation zone can be seen for the velocities from Figure 4. The recirculation zone is longer for the flow at $Re = 6.86 \cdot 10^5$ than for the flow at $Re = 1.36 \cdot 10^5$, as seen from the negative difference in Figure 4c. On further evaluation of the flow separation point over the cylinder, it moves from 100.2° to 107.4°.

3.2. Correction using different a_1

The simulations are now performed for $Re = 2.89 \cdot 10^5$ to analyse the influence of the parameter a_1 along with the Wilcox boundary condition, as suggested in the literature for better flow prediction [9; 19]. Figure 5 shows that as a_1 reduces from the default value of 0.31, the drag coefficient increases drastically. The drag coefficient almost reaches a steady value of approximately 0.72 when a_1 is greater than or equal to 0.34. Figures 3 and 4 show that the over-estimation of the adverse pressure gradient regions leads to a higher drag coefficient, especially at lower Reynolds numbers. Therefore, a higher value of a_1 reduces this over-estimation by

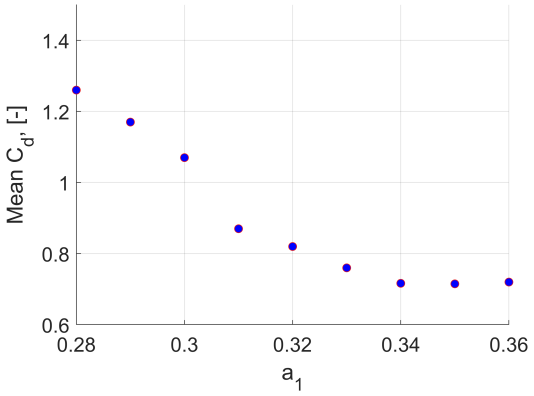

Figure 5: Variation of mean drag coefficient at Reynolds number $Re = 2.89 \cdot 10^5$ for various a_1 using the Wilcox boundary condition.

controlling the SST limiter from Equation (1) at lower Reynolds numbers.

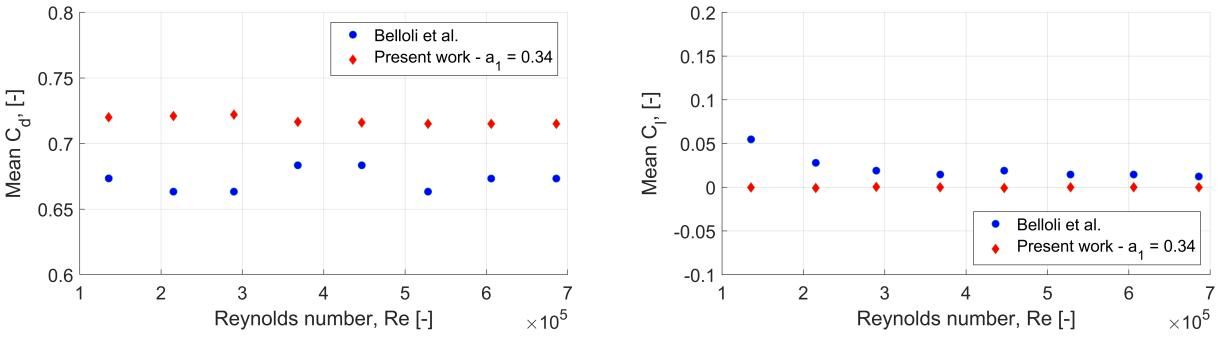

Figure 6: Variation of mean drag coefficient (left) and mean lift coefficient (right) for a fixed cylinder at different Reynolds numbers using the Wilcox boundary condition and $a_1 = 0.34$ compared against experimental data from [2].

The simulations are then carried out with $a_1 = 0.34$ for all flows, such that the flow separation is predicted accurately. Figure 6 shows the results obtained from the simulations with updated variables, and it is in good agreement with the values obtained from the experiment. As observed in the experiment, the drag coefficient is almost the same throughout the Reynolds number range, which corroborates that the flow field could mimick the same scenarios as for the trans-critical Reynolds number regime. The maximum error observed between the values obtained from the simulation and the experiment is 6.5%, which gives sufficient confidence in the numerical model used. There is sufficient agreement with the mean values observed for c_l, which is close to zero for both experiment and simulation. Figure 7b shows the variation of skin friction coefficient, c_f, as the constant a_1 is increased. The transition point from laminar to turbulent region is indicated by an increase in the skin friction coefficient and a drop in the distribution. The figure shows that the transition point shifts from approximately 70° to 62°, imparting more energy into the flow. This effect can be seen in Figure 7a where the pressure recovery happens earlier than the simulations with $a_1 = 0.31$. Furthermore, at low Reynolds number, the base pressure is much lower than of the high Reynolds number, which explains the higher drag coefficient in such cases.

In the experiment conducted in [2], a clear vortex shedding is seen in the wake. The Strouhal frequencies observed for Reynolds numbers $1.35 \cdot 10^5$ and $6.1 \cdot 10^5$ are 0.18 and 0.17, respectively.

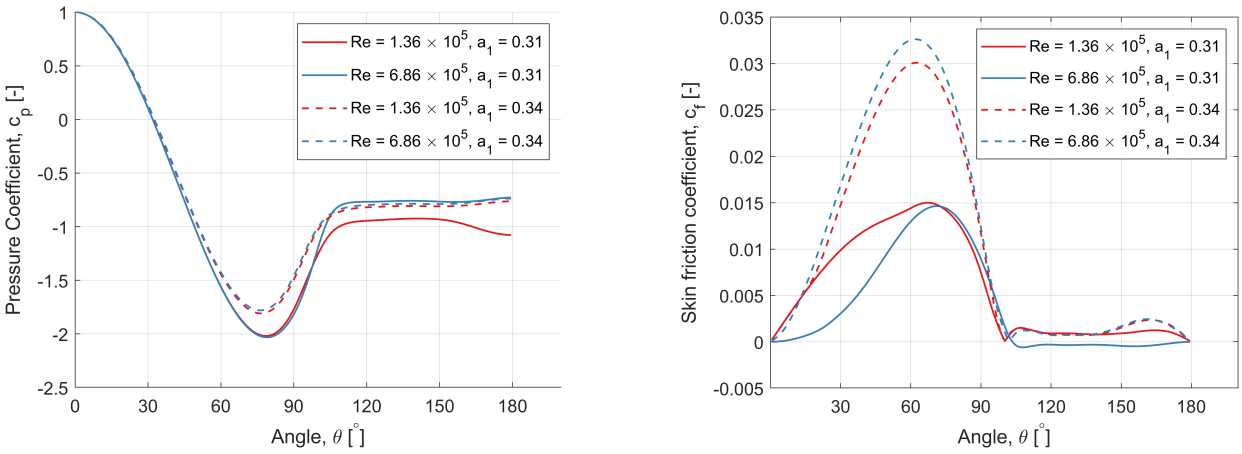

(a) (b)

Figure 7: (a) Pressure coefficient and (b) skin friction coefficient across the cylinder at Re = 1.36×10^5 and 6.86×10^5 for $a_1 = 0.31$ and 0.34.

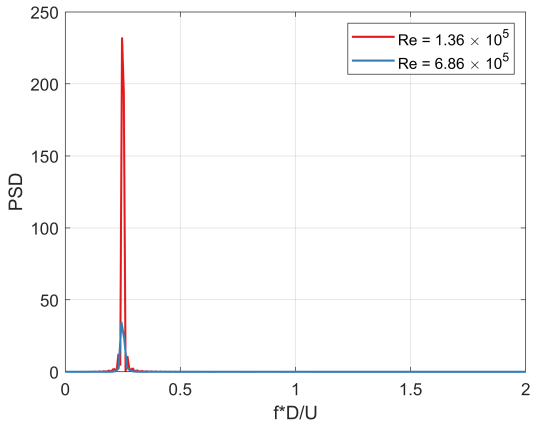

Figure 8: Power spectral density for Reynolds numbers $1.36 \cdot 10^5$ and $6.86 \cdot 10^5$.

Figure 8 shows the power spectral density (PSD) for the same Reynolds numbers. A similar peak in the PSD is seen for both Reynolds numbers, which suggests a strong vortex shedding for these flow conditions. It should be noted that the strength of vortex shedding reduces as the Reynolds number increases, which is seen in Figure 8. The Strouhal number obtained from the simulation is 0.24 for both Reynolds numbers, slightly higher than the Strouhal numbers in the experiment.

3.3. Force-partitioning analysis

The current section shows the preliminary analysis of contributions from various forces partitioned using the methodology mentioned in Section 2.3. The boundary conditions and the numerical parameters used for this analysis is same as that mentioned in Section 3.2. Figure 9 show the contributions from each force for the Reynolds numbers $1.36 \cdot 10^5$ and $6.86 \cdot 10^5$, respectively. Unlike seen from the works of Menon and Mittal [14], the only significant force contributor in these Reynolds number ranges is the vorticity-induced force. As seen in Equation (6), the vorticity-induced force purely arises from the vorticity-dependent variables such as rotational velocity u_ν and vorticity ω. The reason for no other major force is two-

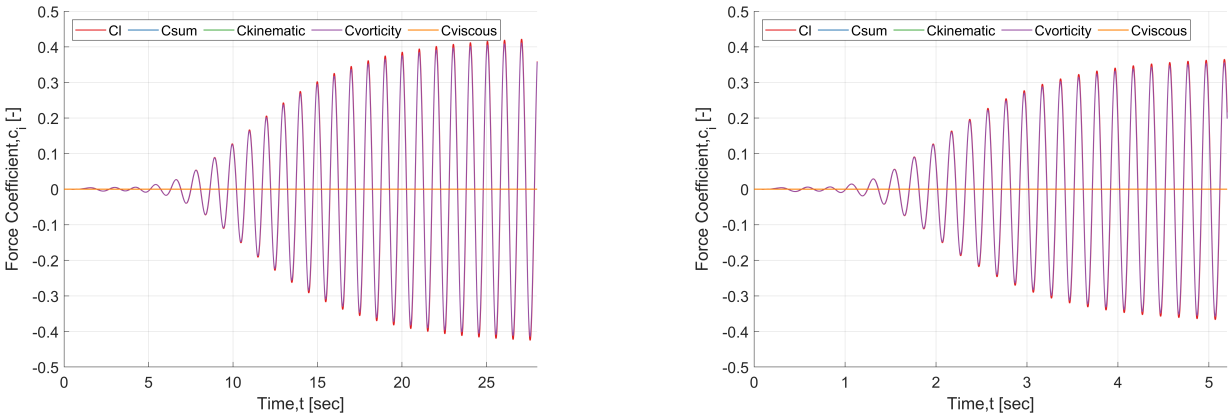

(a) (b)

Figure 9: Comparison of lift force coefficient against the sum of force coefficients from the force-partitioning method for (a) $Re = 1.36 \cdot 10^5$, and (b) $Re = 6.86 \cdot 10^5$.

fold: the cylinder is fixed, and there are no translational or rotational degrees of freedom; the fluid considered for the flow is air, which is a low viscous fluid. This leads to little to no contribution from kinematic and viscous forces, respectively. Yet, this methodology is useful for the application to moving cylinders in future work.

4. Conclusions

In the current study, numerical simulations were carried out to validate the flow over a fixed rough cylinder for Reynolds numbers ranging from $1.36 \cdot 10^5$ to $6.86 \cdot 10^5$. The experiments were conducted to simulate the flow effects similar to the flow over a smooth cylinder at post-critical Reynolds numbers by adding a nylon net over the surface of the cylinder. As obtained from the experimental results, the mean drag coefficients are constant for both the experiment and numerical simulations throughout the wind speeds investigated.

Even though the literature suggests that the k-ω SST turbulence model is able to predict the flow in adverse pressure gradients, it was observed that there was a significant difference for force coefficients in lower Reynolds number ranges over objects with surface roughness. From the works of Gutierrez et al. [9] and Mendez et al. [10], the roughness model with the Wilcox boundary conditions is well-suited for the prediction of aerodynamic characteristics over a rough surface. In addition to this boundary condition, the constant a_1 is varied to predict the flow around uniformly distributed rough surface. As the value for a_1 is increased, the contribution from the SST limiter is reduced, which in turn predicts the flow separation and the aerodynamic coefficients sufficiently accurately.

The method of force partitioning was implemented in OpenFOAM to investigate the various forces contributing to the total force. Depending on the direction in which the forces are partitioned, the sum of all the partitioned forces gives the lift or drag force. But in the current study, the cylinder is considered to be fixed without translational or rotational degree of freedom. Hence, the only force contributor is found to be the vorticity-induced force.

This study investigated the flow over a cylinder section with uniformly distributed roughness and showed its usefulness to mimick higher Reynolds number cases. However, real wind turbine towers are three-dimensional and prone to motion, i.e. the cylinder has translational and possibly even rotational degrees of freedom. As a consequence, the composition of the force partitioning will be different. In order to better carry out more realistic wind tunnel analyses on VIV for wind turbine towers, it is, therefore, beneficial to understand the similarity of flow over smooth

cylinders at trans-critical Reynolds numbers and the flow over rough cylinders also for these more general conditions.

References

[1] Roshko A 1961 *Journal of Fluid Mechanics* **10** 345–356

[2] Belloli M, Giappino S, Morganti S, Muggiasca S and Zasso A 2015 *Ocean Engineering* **94** 140–154 ISSN 0029-8018

[3] Buresti G 1981 *Journal of Wind Engineering and Industrial Aerodynamics* **8** 105–114 ISSN 0167-6105

[4] Zdravkovich M 1997 *Flow Around Circular Cylinders Volume I: Fundamentals* (Oxford University Press)

[5] van Hinsberg N P 2015 *Journal of Fluids and Structures* **55** 526–539 ISSN 0889-9746

[6] Gao Y, Zong Z, Zou L, Takagi S and Jiang Z 2018 *Marine Structures* **57** 165–179 ISSN 0951-8339

[7] Chen W, Wang S, Shi X, Rheem C K, Lin Y and Liu E 2022 *International Journal of Naval Architecture and Ocean Engineering* **14** 100430 ISSN 2092-6782

[8] Rafael C F, Pio D M and da Silva G A L 2015 *SAE Technical Paper*

[9] Gutierrez R, Zamponi R, Ragni D, Llorente E and Aranguren P 2023 *Wind Energy* **26** 650–667

[10] Mendez B and Munduate X 2015 *Study of distributed roughness effect over wind turbine airfoils performance using CFD* (American Institute of Aeronautics and Astronautics) AIAA SciTech Forum

[11] Hellsten A, Laine S, Hellsten A and Laine S *Extension of the k-omega-SST turbulence model for flows over rough surfaces*

[12] Knopp T, Eisfeld B and Calvo J B 2009 *International Journal of Heat and Fluid Flow* **30** 54–65 ISSN 0142-727X

[13] Viré A, Derksen A, Folkersma M and Sarwar K 2020 *Wind Energy Science* **5** 793–806

[14] Menon K and Mittal R 2021 *Journal of Fluid Mechanics* **907** A37

[15] Openfoam-v2012 `https://www.openfoam.com/news/main-news/openfoam-v20-12`

[16] Menter F R, Kuntz M and Langtry R 2003 *Turbulence, heat and mass transfer* vol 4 pp 625–632 ISBN 1567001963

[17] Johnson D A and King L S 1985 *AIAA Journal* **23** 1684–1692

[18] Menter F R 1994 *AIAA Journal* **32** 1598–1605

[19] Matyushenko A A and Garbaruk A V 2016 *Journal of Physics: Conference Series* **769** 012082

[20] Quartapelle L and Napolitano M 1983 *AIAA Journal* **21** 911–913

[21] Zhang C, Hedrick T L and Mittal R 2015 *PLoS ONE 10(8): e0132093*

[22] Batchelor G K 2000 *An Introduction to Fluid Dynamics* Cambridge Mathematical Library (Cambridge University Press)

[23] VimalKumar S, De Tavernier D, von Terzi D, Belloli M and Viré A 2024 *Wind Energy Science Discussions* **2024** 1–24 URL `https://wes.copernicus.org/preprints/wes-2024-10/`